ENSO Effects on Gulf of Alaska Eddies

Arne Melsom,* Steven D. Meyers, Harley E. Hurlburt,† Joseph E. Metzger,† and James J. O'Brien****

*Norwegian Meteorological Institute, Oslo
**Center for Ocean–Atmospheric Prediction Studies, The Florida State University, Tallahassee, Florida
†Naval Research Laboratory, Stennis Space Center Mississippi

Received 22 May 1998; accepted 3 February 1999.

ABSTRACT: Generation and propagation of eddies in the coastal regions of the eastern Gulf of Alaska are examined based on ouput from a numerical ocean model. Results from a 1/8° six-layer isopycnal, wind-forced Pacific basin model are examined within the Gulf of Alaska during the 14-yr period starting in January 1981. Interannual variability in the upper ocean coastal circulation in the Gulf of Alaska is linked to the El Niño–Southern Oscillation phenomenon in the tropical Pacific Ocean, via coastal Kelvin waves and atmospheric teleconnections. El Niño events destabilize the Alaska Current by enhancement of the velocity shear in the vertical. The instability ultimately results in the formation of multiple strong anticyclonic eddies along the coast, which slowly propagate into the Gulf of Alaska where they can survive for more than 1 yr. A typical value for the diameters of the anticyclonic eddies is 200 km in the data and in the model. These eddies are strongly baroclinic, with a typical value for the velocity differences between layers 1 and 2 of 15 cm s^{-1}. El Viejo (La Niña) events generally reduce eddy formation.

* Corresponding author address: Arne Melsom, Norwegian Meteorological Institute, P.O. Box 43, Blindern, N-0313 Oslo, Norway
E-mail address: arne.melsom@dnmi.no
**Current affiliation: Department of Marine Science, University of South Florida, St. Petersburg, Florida

KEYWORDS: Numerical modeling; Eddies and mesoscale processes; El Niño; Sea level variations

1. Introduction

The continental slope of the northeast Pacific is a major habitat for a number of commercially harvested fish (e.g., salmon, halibut, and herring) (Cummins and Mysak, 1988). It has been suggested that year-to-year changes in fish stock recruitment and return migration routes of certain species in the Gulf of Alaska (GOA) are affected by low-frequency ocean variability such as the El Niño–Southern Oscillation (ENSO) (Emery and Hamilton, 1985; Mysak, 1985). ENSO affects the extratropical oceans in two ways: locally, through changes in the surface winds, and, remotely, via tropically generated, coastally trapped Kelvin waves. Although the effect on the ocean circulation by surface winds is local, the surface wind may in itself be remotely forced by atmospheric wave motions.

Kelvin waves associated with El Niño warm events suppress upwelling of denser and nutrient-rich water masses, and those associated with El Viejo (La Niña) cold events enhance such upwelling. Both alter the biogeochemical cycle of the coastal northeast Pacific Ocean. These large changes should induce changes in the biological productivity. ENSO has been tied to changes in zooplankton biomass (McGowan, 1985; Smith, 1985) in the California Current system and interannual changes in coastal upwelling have been linked to variations in the population and health of several species of fish (Ware and Thomson, 1991). A similar relationship might be expected in the GOA.

Kelvin waves are an important oceanic teleconnection mechanism between the Tropics and higher latitudes. Theoretical (Moore, 1968) and numerical (Pares-Sierra and O'Brien, 1989) ocean models show that tropically generated Kelvin waves are a significant source of interannual variability of the nearshore ocean circulation along western America, as well as the generators of large-amplitude Rossby waves in the midlatitude Pacific basin (Johnson and O'Brien, 1990; Jacobs et al., 1994), which play a vital role in decadal climate variability (Meyers et al., 1996).

Detecting these Kelvin waves has proven difficult. Poleward propagating waves at interannual timescales associated with El Niño have been found, but these waves were only at intraseasonal timescales (Enfield and Allen, 1980; Chelton and Davis, 1982; Spillane et al., 1987). This has led to the neglect of the Kelvin wave as a powerful mechanism of oceanic variability, particularly at the higher latitudes of the Pacific Ocean. However, more recent analysis of temperature and sea level data has shown that Kelvin waves generated during extremes of ENSO can propagate from the tropical Pacific up the west coast of North America to the Aleutian Island chain (Norton and McLain, 1994; Meyers et al., 1998), and the Kamchatka Peninsula (Smedstad et al., 1997; Metzger et al., 1998). Ramp et al. (Ramp et al., 1997) showed sea level along the western coast of North America during the 1991 El Niño was characterized by a northward propagating signal originating in the Tropics and a southward signal originating in the

GOA. The former was attributed to a coastally trapped Kelvin wave and the latter to wind forcing. Wind anomalies outside the Tropics (Wallace and Gutzler, 1981) are another source of ENSO-induced variability in the ocean circulation.

The general ocean circulation in the GOA is dominated by the cyclonic Pacific subpolar gyre, as revealed by dynamic topography charts (Lagerloef, 1995). The current associated with this gyre forms the Alaska Current (AC), a broad and weak eastern boundary current flowing northward in the eastern GOA. The AC becomes narrower and stronger as it approaches the northern GOA, ultimately leaving the region as the Alaskan Stream, an intense southwestward flowing current along the southern coast of Alaska (west of the panhandle) and the Aleutian Islands chain. Furthermore, there is a wave guide at the eastern margin of the GOA where the flow is highly variable due to variations in wind forcing and coastally trapped waves propagating in from the south (Chelton and Davis, 1982).

In this investigation, we examine the results from a 1/8° six-layer isopycnal model with realistic coastline geometry and bottom topography. For model details, see Hurlburt et al. (Hurlburt et al., 1996). The numerical simulation is driven by realistic daily wind stress from 1981 to 1994. An annual cycle of eddy activity is found in the ocean circulation of the eastern GOA. This numerical experiment indicates strong interannual variability in this region. The existence of these seasonal and interannual variations is supported by observations of the ‘‘Sitka eddy’’ (Tabata, 1982).

2. The ocean model

The model results are made available by the Naval Research Laboratory (NRL), Stennis Space Center, Mississippi. The model experiment is a multilayer Pacific basin simulation using the NRL Layered Ocean Model (NLOM) (Wallcraft, 1991). NLOM is based on the semi-implicit, free surface model of Hurlburt and Thompson (Hurlburt and Thompson, 1980), and it is formulated using an Arakawa C grid (Arakawa, 1966). The daily 1000-mb wind product from the European Centre for Medium-Range Weather Forecasts (ECMWF) [with the 1981–91 mean replaced by the Hellerman and Rosenstein (Hellerman and Rosenstein, 1983; hereafter, HR) annual mean] drives the ocean circulation. Recent results from this class of models and additional model description are given by Hurlburt et al. (Hurlburt et al., 1996).

The model includes realistic bottom topography from a modified version of the 1/12° ETOP05 (NOAA, 1988) bathymetric product. The topography dataset was first interpolated to the model grid and then smoothed with a nine-point smoother. This is to reduce the energy generation at small scales that are poorly resolved by the model. In the model integration, the amplitude of the topography above the maximum depth of 6500 m was multiplied by 0.8 to confine it to the lowest layer. The model includes realistic coastline geometry, determined by the 200-m depth contour of the ETOP05 topography that represents the shelf break. The ETOP05 and model topography is displayed in Figure 1.

The Pacific model domain extends from 20°S to 62°N and has a horizontal resolution of 1/8° × 45/256° (lat × long) for each variable, which is approxi-

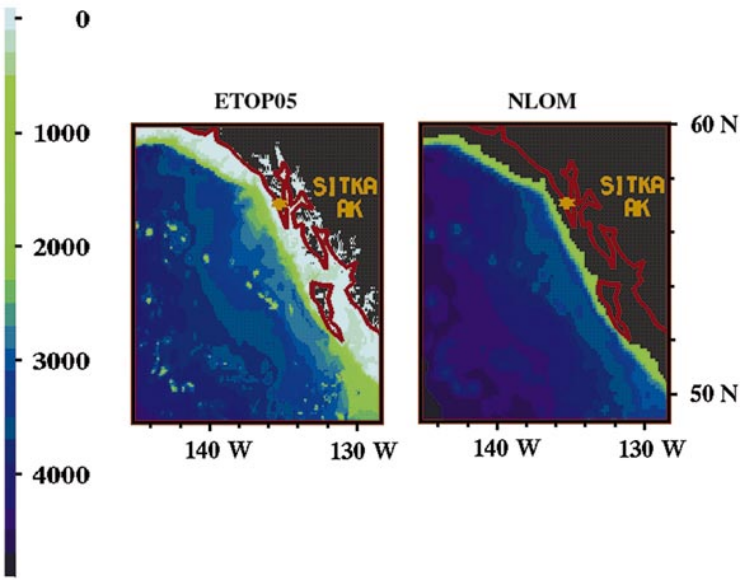

Figure 1. Ocean depth in the eastern Gulf of Alaska. The 1/12° ETOP05 bottom topography and the topography used in the NLOM simulation are shown in the left and right panels, respectively. See the text for a detailed description of the relation between the two. The color coding of the depth (in m) is shown to the left.

mately 14 km × 10 km in the Alaska Gyre region. Isopycnal outcropping is an essential feature of ocean models covering the GOA. This is included by entrainment from the layer below whenever a layer becomes thinner than a prescribed minimum thickness. Mass is conserved within the layers, so that an accumulation of entrained mass in one layer is balanced by an equal amount of detrained mass elsewhere in the model domain; see Shriver and Hurlburt (Shriver and Hurlburt, 1997) for a detailed discussion.

The model was spun up to a statistical equilibrium using the HR monthly mean wind stress climatology. Subsequently, the model was forced for a 14-yr period (1981–94) starting 1 January 1981 with daily 1000-mb winds from the ECMWF with the long-term mean replaced by HR. While the model domain is the Pacific Ocean north of 20°S, the model subdomain examined here is the eastern GOA bounded by 46°N in the south and 145°W in the west. Only the results obtained for the two uppermost layers are discussed since these contain the essential dynamics of the upper ocean circulation. Movie 1 displays the mean annual cycle of the upper layer thickness.

3. Model results

3.1. General circulation and eddy formation

In the model GOA, the thicknesses of the first and second layers are typically 50–60 m and 50–150 m, respectively. However, there are frequently large devi-

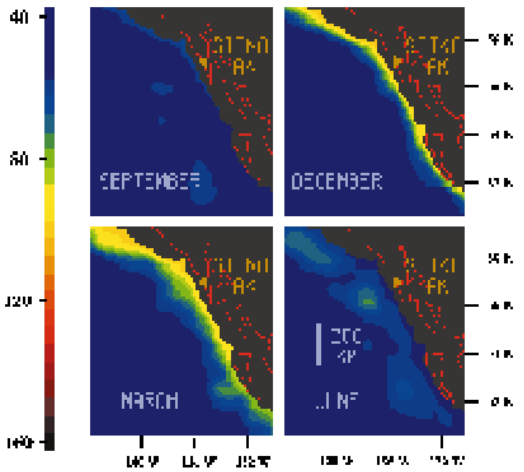

Movie 1. The mean annual cycle of the upper-layer thickness in the eastern Gulf of Alaska.

See the online version of this paper to view animation.

ations from these means. Along the coast, the interface between the upper two layers can be deflected up to 100 m below its local mean depth. Outside the coastal region, this deflection may have the same deviation magnitude at the center of westward drifting eddies. A poleward flowing current corresponding to the AC is observed in the simulation results. The model AC has a seasonal cycle similar to that reported by Lagerloef et al. (Lagerloef et al., 1981), who attributes the cycle to a seasonal shift in the atmospheric circulation from the intense Aleutian low during winter to the North Pacific high pressure system during summer (Royer, 1975). In the model, the transport, upper layer thickness, and vertical shear of the velocity associated with the coastal current reach maximum values in December or January. At this time, the magnitude of the velocity differences between layer 1 and layer 2 is typically 10 cm s^{-1} in coastal regions (approximately 15 and 5 cm s^{-1} in layers 1 and 2, respectively), with maximum values exceeding 40 cm s^{-1}.

In most winters the model AC meanders. The alongshore wavelength and offshore amplitude of the meanders are typically 200 km and 40 km, respectively. However, the amplitude may become ~100 km, after which the current usually breaks into predominantly anticyclonic eddies. The eddies are seen to drift slowly southwestward (i.e., offshore), with an estimated speed of ~1 cm s^{-1}, or ~300 km yr^{-1}. Generally, the horizontal pressure gradient is significantly larger in layer 1 than in layer 2. Hence, the accompanying velocity shear is significant and the motion in the meanders is strongly baroclinic.

Fewer cyclonic eddies are generated and they decay more rapidly. The generation of cyclonic eddies may be artificially suppressed due to their relatively small horizontal extent, since horizontal gradients are dampened by a Laplacian friction that selectively dampens small scales. (This is necessary for numerical

stability.) Further, the production of cyclonic eddies may be reduced due to the limited space inshore of the current. Cyclonic eddies may also be weakened by the isopycnal outcropping in the model, since such outcropping reduces thickness gradients of shallow model layers. The thickness gradients are the model's representation of the horizontal density gradients. Isopycnal outcropping is characteristic of this region.

3.2. Instability processes

Instability processes at the oceanic mesoscale are traditionally divided into barotropic and baroclinic instability. Barotropic instability is the process where mesoscale features (meanders, filaments, eddies) develop from a basic state by conversion of kinetic energy from the basic state to the eddy field (Rayleigh, 1880; Kuo, 1949; Fjortoft, 1950). In the case of an *f* plane, a necessary condition for instability is the presence of an inflection point in the basic-state flow. In contrast, baroclinic instability is the process in which energy is converted from (basic state) potential energy to mesoscale energy (Eady, 1949; Phillips, 1951). In a two-layer system, the wavelength of the most rapidly growing disturbance is a function of mean flow, velocity shear in the vertical, buoyancy, layer thickness, and latitude.

The instability mechanism is investigated here by examination of a cross section at 56.75°N. Using the surface elevation and deflection of the interface between layers 1 and 2 as the basic state on a straight geostrophic *f*-plane channel, the growth rate of unstable perturbations may be found.

By a modified version of Phillips's theory for a two-layer system as described in appendix A, baroclinic instability is investigated. The theory is easy to apply, but the gross simplifications implied must be kept in mind when discussing the results thereof. Growth rates computed from the model cross section on 28 January 1983 are depicted as a function of wavenumber by the blue line in Figure 2.

The stability of the cross section may be studied in more detail by solving an eigenvalue/eigenvector problem using a finite difference formulation for perturbation variables (EV analysis); this is also described in appendix A. Assuming a two-layer system, the growth rates computed by this method are depicted as a function of wavenumber by the green line in Figure 2. From Figure 3 we note that the growth rate of perturbations increases by almost a factor of 2 from 22 January to 3 February 1983. This is probably due to potential energy added by the local winds, or a combination of this and a deepening of the Kelvin signal.

Results of the EV analysis from a selected period are displayed in Figure 3. The perturbations with the highest growth rates have wavelengths of around 200 km, which is in concord with the sizes and spacing of the anticyclonic eddies that are generated. On the other hand, the highest growth rate perturbations as computed by Phillips's theory have wavelengths of approximately 100 km, in discord with the evolving eddies. Since Phillips's theory only involves baroclinic instability, whereas the EV analysis also incorporates barotropic instability, this study indicates that the model eddies are triggered by mixed (barotropic/baroclinic) instability. Moreover, the exponential growth rate of ~1/(11.5 days) in the EV analysis also corresponds well to the duration of the eddy genesis; see Figure

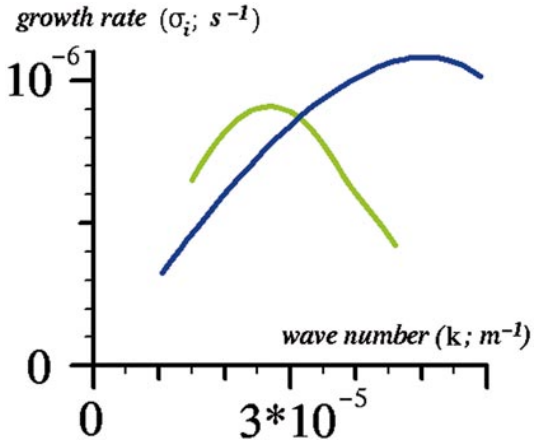

Figure 2. Perturbation growth rate as a function of wavenumber on 28 January 1983. Application of Phillips's theory is displayed by the blue line; results from an eigenvalue/eigenvector method are shown by the green line. Computations are based on the model cross section at 56.75°N off the American continent. See appendix A for details on the instability analysis.

4. The EV analysis also yields that the the interface perturbation amplitude is 300 times the amplitude of the surface perturbation.

The EV analysis was repeated for a case of downwelling in November 1988, that is, during the 1988–89 El Viejo episode. The cross section at 56.75°N was again investigated, and the result of the analysis is that the perturbations with the highest growth rates have wavelengths of around 100 km. In the present simulation, one wavelength is then spanned by seven grid nodes, and the numerical damping of small horizontal scales will have a negative effect on the generation of eddies. The growth rate on 7 November 1988 is displayed as a function of wavenumber in Figure 5 (top) where it is compared to the results for 28 January 1983. Also in Figure 5 (bottom), the duration of the unstable perturbations is depicted. Here, the red line shows the growth rate of the 200-km-long wave perturbation in 1983, and the blue line is the corresponding development of the 100-km-long wave perturbation in 1988. Note the relatively small changes of high growth rates in the 1983 case, which indicates that instability-favorable conditions lasted for at least two *e*-folding periods of 11.5 days.

Feliks and Ghil (Feliks and Ghil, 1993) performed a detailed instability analysis of a downwelling front along the southern coast of Asia Minor in the eastern Mediterranean. They found that the *f*-plane approximation worked well until eddies had developed, except for cases with very small basic-state currents. They also found that increasing the number of vertical modes beyond two does not significantly affect the most unstable wave. This explains the relative success of the fairly simple EV analysis above.

We end this discussion by noting that the present analysis is unfit to describe

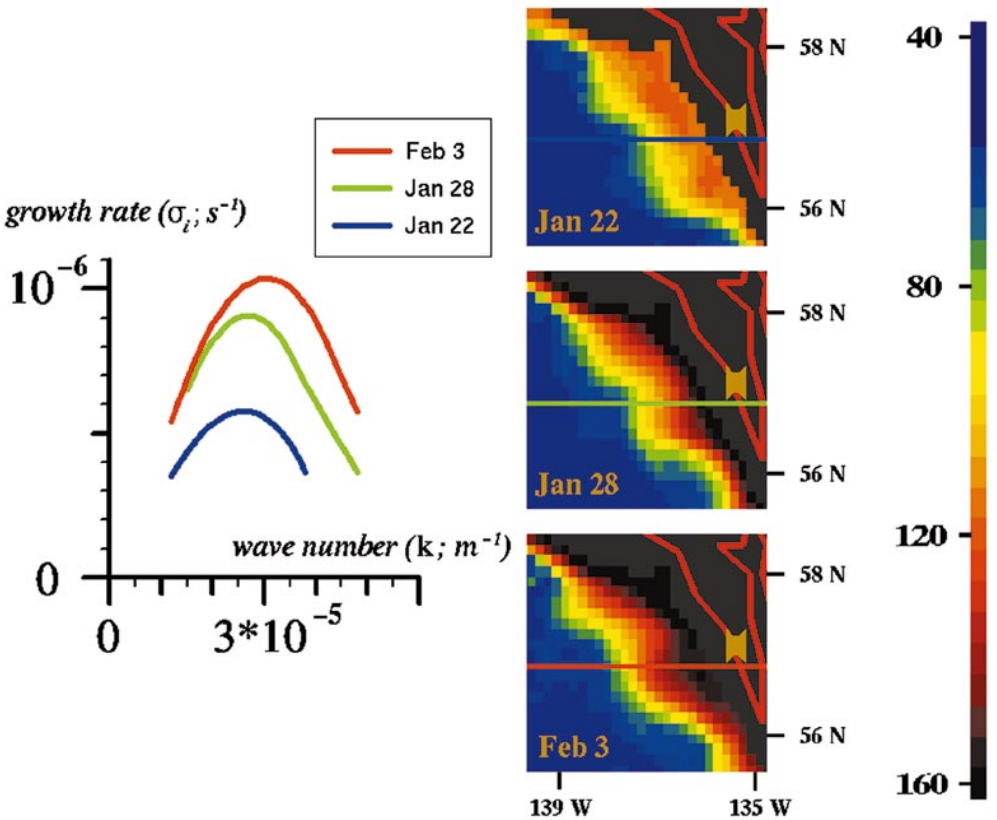

Figure 3. (left) Perturbation growth rate as a function of wavenumber during the 1982–83 model Sitka eddy generation, as computed by an eigenvalue/eigenvector method. Computations are based on the model cross section at 56.75°N off the American continent, indicated by straight colored lines in the snapshots. See the appendix for details on the instability analysis. (right) Snapshots of the upper-layer thickness in the model for the three dates in 1983 under consideration. The brown marks indicate the position of Sitka, AK. Color coding of upper-layer thickness is given by the bar to the far right (in m).

the later stages of the eddy generation, and their eventual drift westward. Anticyclonic eddies will become larger, and cyclonic eddies become smaller, due to nonlinear (semigeostrophic) effects, as described by Hoskins (Hoskins, 1975). This is also observed in the model results; see, for example, Movie 3 below.

3.3. ENSO effects

ENSO events may be characterized by extreme values of an index such as the Southern Oscillation index (a proxy measure of El Niño based on surface air pressure differences between Darwin, Australia, and Tahiti, French Polynesia) (Walker, 1928), or large SST and sea surface height (SSH) anomalies in the

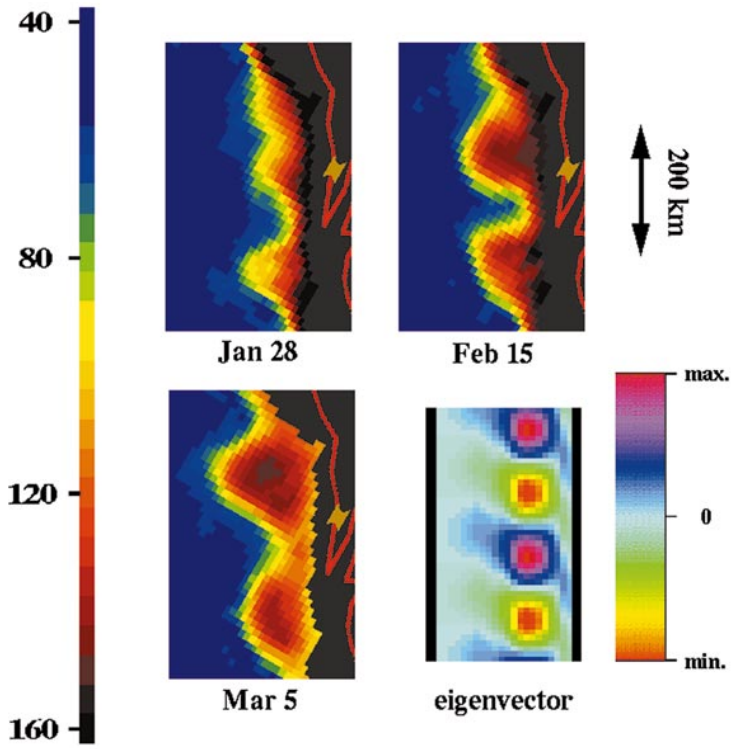

Figure 4. Model snapshots, and eigenvector solution, for upper-layer thickness. The snapshots have been rotated 30° clockwise from their usual orientation (with west to the left, etc.). The brown marks indicate the position of Sitka, AK. Snapshot color coding of upper-layer thickness is given by the bar to the left (in m). The eigenvector is the EV analysis result of the 28 January cross section. The color bar for the eigenvector solution is displayed in the bottom-right frame. The cross section is depicted by the green line in Figure 3, 28 January snapshot.

eastern tropical Pacific Ocean. Figure 6 shows the anomalous deflection of the interface between the second and third layers in the model following an El Niño and an El Viejo. This indicates an ENSO influence on the GOA ocean circulation. These anomalous deflections along the coast of 50–80 m are substantial compared to the mean depth of the upper two model layers of ~170 m. Therefore the ENSO effect is significant in this area.

One of the two major El Niño events in recent history occurred during the 1982–83 boreal (northern) winter (the other event being that of 1997–98). The most intense eddy formation event in the model run occurs at this time. Movie 2 displays the eddy generation in the GOA following the 1982–83 event. In the movie, the evolution of the model upper layer is shown and Lagrangian vectors for the circulation of the upper layer are included. The evolution and offshore propagation of the eddies that are generated in Movie 2 are animated in Movie

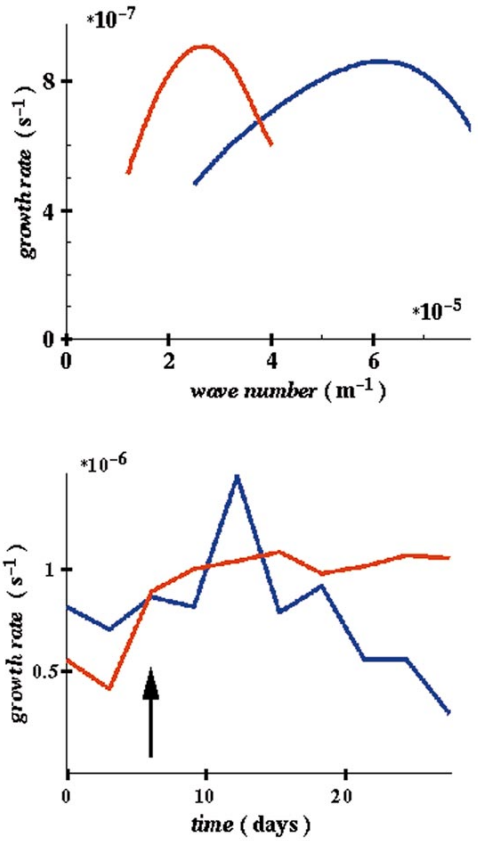

Figure 5. Perturbation growth rates as functions of wavenumber (top) and time (bottom) for a cross section at 56.75°N. (top) The results from the EV analysis for 28 January 1983 and for 7 November 1988 are displayed by the red and blue lines, respectively. (bottom) The temporal evolution of the maximum growth rates. Here, the red line depicts growth rates from 22 January 1983 for a 200-km perturbation, and the blue line shows the growth rates from 1 November 1988 for a 100-km perturbation. The arrow in the bottom panel indicates the dates that correspond to the top panel.

3. One observes that the anticyclonic eddies remain as the dominating feature of the Gulf of Alaska ocean circulation throughout 1983. In 1984, the model circulation in the GOA is dominated by the lasting effect of the strong eddies that were generated the year before.

Another striking feature of the model results is the pronounced baroclinicity of the eddies. This property yields strong velocity shears in the vertical. Movie 4 presents the velocity difference from layer 1 to layer 2 during 1983. The rings of strong vertical shear in the velocity at the eddy rims are typical for baroclinic eddies.

Model results indicate that upwelling perturbations stabilize the flow and

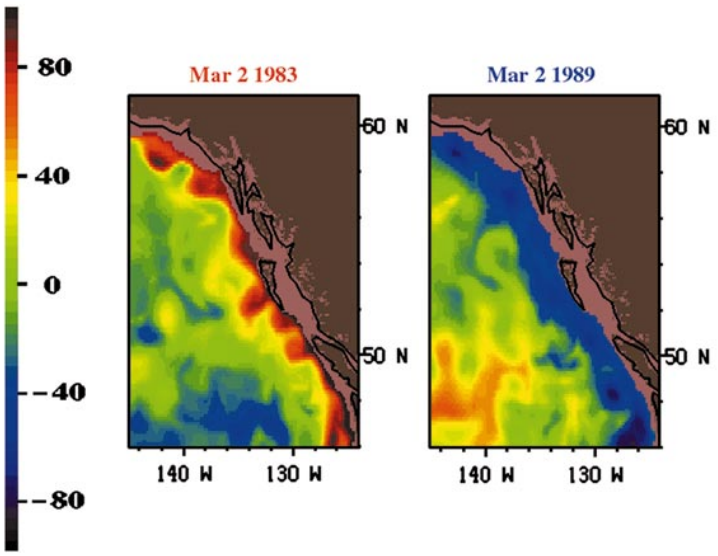

Figure 6. ENSO signal in the Gulf of Alaska from the simulation. The ocean circulation in the Gulf of Alaska following the 1982–83 El Niño in the tropical Pacific Ocean is shown on the left-hand side. The situation following the 1988–89 El Viejo event (La Niña) is displayed to the right. Both depictions show the situation on 2 March (1983 and 1989). The colors indicate the thickness anomaly of the two upper layers relative to the seasonal mean. Yellow and red colors show regions with anomalously deep layers, blue and purple colors correspond to anomalously shallow layers, and green colors indicate values close to the mean.

yield few and weak eddies. There are two El Viejo events (Meyers et al., 1999) during the model study: late 1984 and early 1988. No deep eddies are generated during the 1988 event. Figure 6 (right panel), however, clearly shows the generation of some cyclonic eddies (although not as apparent given the choice of color scales). Mesoscale motion is also weak following the 1984 event. (The 1984 El Viejo was of moderate size and is not recognized as an ENSO event by all indices.) Eddy generation is common during the winter and the sparsity of eddies suggests these ENSO events may suppress normal eddy development. Movie 5 displays the thickness of the upper layer in the model following the 1988–89 event. Some upper-layer anticyclones of relatively small size can be seen in this animation.

4. Comparison to observations

4.1. Sea surface height

We compare observations of SSH at Sitka, Alaska, and model results at the closest model node. The position of Integrated Global Ocean Services System (IGOSS)

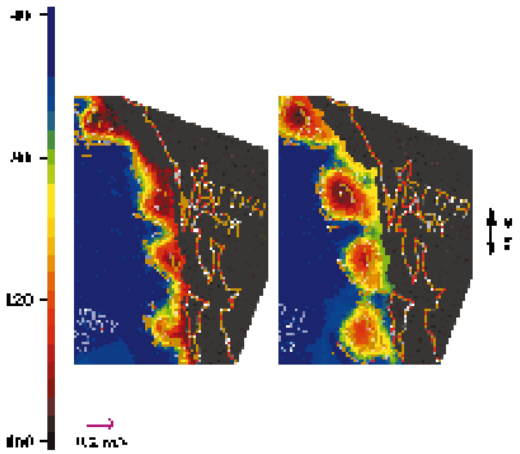

Movie 2. Model eddies in the GOA after the 1982–83 El Niño.

See the online version of this paper to view animation.

sea level station Sitka is indicated by a full pink circle in Figure 7 (57.05°N, 135.34°W). Model SSH was extracted at 57°N, 136.09°W (full yellow circle).

The model results have been sampled at a frequency of 1/(3.05 days). Hence, we interpolate the daily SSH observations to model output dates using a low-pass boxcar filter (LPB filter). In Figure 8a, the resulting SSH anomalies for a 1-yr period centered at 1 January 1983 are depicted. The observed SSH values exhibit much larger fluctuations than the model results. This discrepancy is likely

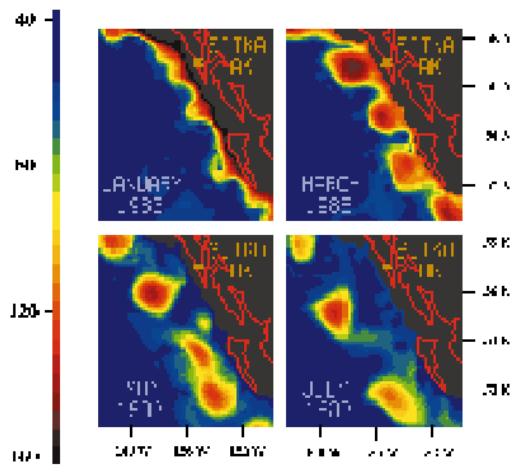

Movie 3. Offshore propagation of eddies from spring to summer 1983.

See the online version of this paper to view animation.

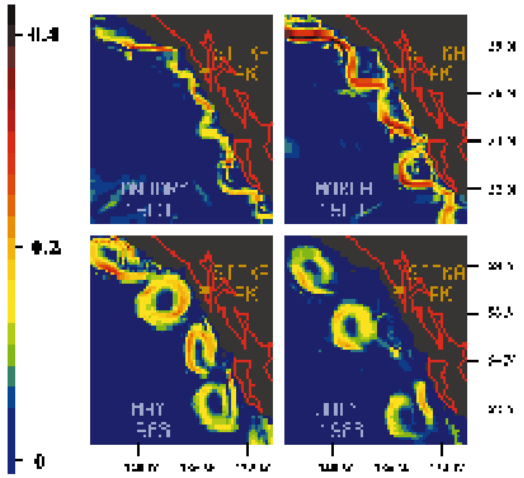

Movie 4. Meandering of the coastal jet in the GOA after the 1982–83 El Niño.

See the online version of this paper to view animation.

due to the exclusion of the continental shelf in the model domain. Thus, generation of shelf waves are suppressed in the numerical model, if not eliminated. Inclusion of these waves is instrumental in the onshelf description of SSH during storm surges (Martinsen et al., 1979).

In order to discriminate the high-frequency onshelf fluctuations, the SSH

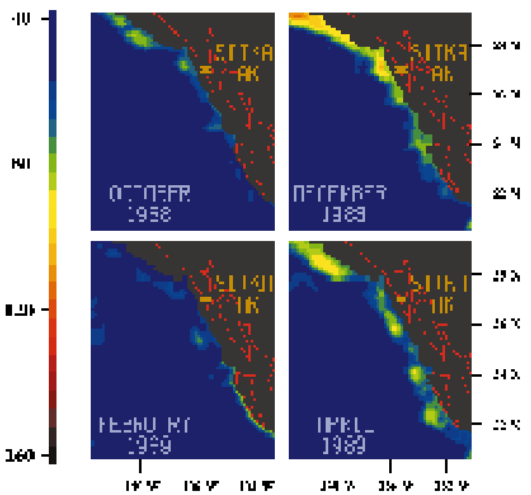

Movie 5. Weak GOA eddies after the 1988–89 El Viejo.

See the online version of this paper to view animation.

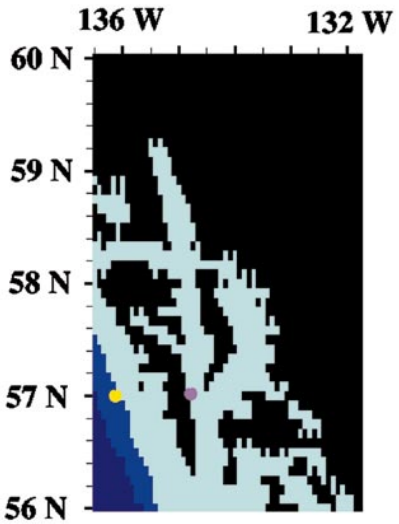

Figure 7. Position of IGOSS sea level station Sitka, AK (full pink circle), and model point Sitka (full yellow circle). The color code indicates land (black), the continental shelf (500 m, light blue), continental slope (blue), and deep ocean (2000 m, dark blue). The depiction has been made from ETOP05 5′ × 5′ navy bathymetry.

time series were subjected to a 2-month LPB filter for the same period. The resulting SSH variations are depicted in Figure 8b. This figure clearly demonstrates the accuracy of the model results. However, the model SSH is unquestionably lagging the data. The highest correlation is achieved with a lag of 12–18 days, when the correlation exceeds 0.99, whereas the no-lag correlation is 0.94. (The corresponding correlation values in the nonfiltered case are 0.78 at a lag of 3 days, and 0.72, respectively.) Note also that the 1982–83 SSH mean is well above the zero level (which is equal to the 1981–94 mean value). This figure depicts the period where the model–observation correlations reach their highest values; see Table 1.

The lag in Figure 8b may arise because the seasonal variations at IGOSS station Sitka are influenced by changes in freshwater drainage by the Alaska Coastal Current and by steric sea level changes. Neither of these effects are included in the present numerical model. The discrete set of wave propagation speeds in the model may also contribute to the lag.

From Table 1, we see that the 2-month LPB filtered correlations are usually between 0.85 and 1. However, it is obvious that the model is unsuccessful in reproducing the observed interannual SSH variability in 1988–89 when the correlation drops to 0.33. The reason for this discrepancy lies mainly in inaccurate model reproduction of two strong spikes in the observed SSH for this period. A positive anomaly of more than 30 cm is observed in November 1988, and a negative anomaly reaching almost 40 cm is measured in February 1989. By ex-

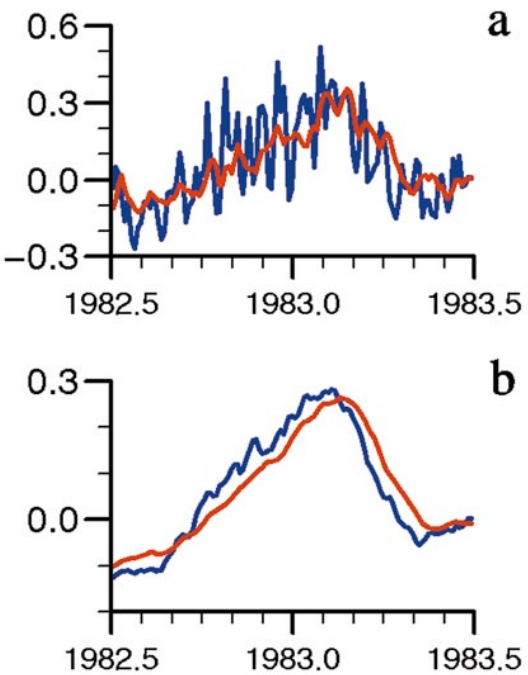

Figure 8. Observed (blue) and modeled (red) SSH anomaly at Sitka, AK, for 1 yr centered at newyear 1983. (a) The results for every third day and (b) the results after applying a 2-month low-pass boxcar filter. Numbers on the vertical axes denote SSH anomalies in m. Anomalies have been computed by subtraction of the 1981–94 mean.

amination of the 2-month LPB filtered time series, we find that the model lags the observed positive anomaly by about half a month, and leads the negative anomaly by approximately one month. Furthermore, the amplitudes of the modeled spikes are much smaller than what the observations reveal. This combination leads to the low correlation value for 1988–89.

From Table 1, we also note the substantial model-data lag at which the highest correlation value occurs in 1989–90. The model has also been run using the National Centers for Environmental Prediction's (NCEP) reanalysis winds. Using this alternative forcing, the model-data intercomparison for 1989–90 is more favorable. However, results for some of the other years are better with the present forcing by ECMWF winds. Thus, the main source of inaccurate model results for SSH is most likely the quality of the forcing fields, that is, the winds. Another possible source for model errors with respect to negative SSH anomalies is the model's management of thin layers by discrimation of sharp coastal fronts in regions of strong upwelling. This may lead to coastal gradients that are too small in the model results, and the largest misrepresentation occurs at the coast.

We end this discussion by noting that the model upper-layer thickness is strongly correlated to the model sea level at seasonal timescales. The no-lag

correlation of the nonfiltered time series is 0.940, and the correlation of the 2-month LPB filtered time series is 0.943. However, at interannual timescales the correlation between upper-layer thickess and sea level is smaller. After application of a 1-yr LPB filter, this correlation is 0.783.

4.2 Eddies

Strong eddy formation due to a propagating internal Kelvin signal also seems consistent with observations. In an extensive examination of oceanographic data collected during 1927–77 in the GOA, Tabata (Tabata, 1982) concluded that ''baroclinic eddies occur frequently in this region. Among these is the recurring, well developed, anticyclonic eddy situated within a few hundred kilometers of Sitka,'' now commonly called the Sitka eddy. The primary characteristics of the Sitka eddy are reproduced qualitatively and quantitatively by the numerical model (diameter 150–300 km, isopycnal deflection of up to 100 m, initial location ~200 km off Baranof Island, lifetime of order 1 yr).

Previous studies have hypothesized that the interannual variability in the GOA may be affected by ENSO events in the tropical Pacific Ocean (Emery and Hamilton, 1985; Mysak, 1985). Although such a link is not discussed by Tabata, the observations of the Sitka eddy indicate interannual variability.

Tabata (Tabata, 1982) refers to the possible presence of the Sitka eddy with various degrees of certainty. The uncertainty may be attributed to the sparsity of available data as well as interannual variability of the mesoscale ocean circulation off Sitka. As can be seen from Figure 9, the simulation results contain a significant amount of interannual variability in this region.

In the datasets that are surveyed by Tabata (Tabata, 1982), the spring of 1958, the summers of 1960 and 1961, and the spring of 1977 are the times when the Sitka eddy was undoubtedly present. Both 1957–58 and 1976–77 were seasons with an El Niño event in the tropical Pacific Ocean.

Repression of eddy activity following El Viejo tropical events is supported by the measurements off Sitka. There are two such events reviewed in Tabata (Tabata, 1982), which occurred in 1955–56 and 1956–57. In the spring and summer of 1956 and 1957, Tabata concludes that the Sitka eddy is either weak or nonexistent.

The simultaneous presence of multiple anticyclonic eddies in the GOA similar to the present results from the NLOM (e.g., Movie 5) was recently established from observations by Thomson and Gower (Thomson and Gower, 1998). Examinating thermal imagery from the winter of 1995, they detected five well-defined warm eddies along the coast from just south of Queen Charlotte Islands in the south to the apex of the GOA in the north. The diameter of the eddies was approximately 160 km, and they were spaced about 250 km apart. Thomson and Gower (Thomson and Gower, 1998) attribute the eddy generations to strong velocity shears in the vertical due to a sudden wind reversal. In the tropical Pacific Ocean, 1994–95 was an El Niño event according to some indices, but not all.

A large deflection of the interface below the upper layer is an important anomaly associated with baroclinic eddies. The response at the surface is the opposite anomaly; that is, downwelling and anticyclonic baroclinic (deep) eddies

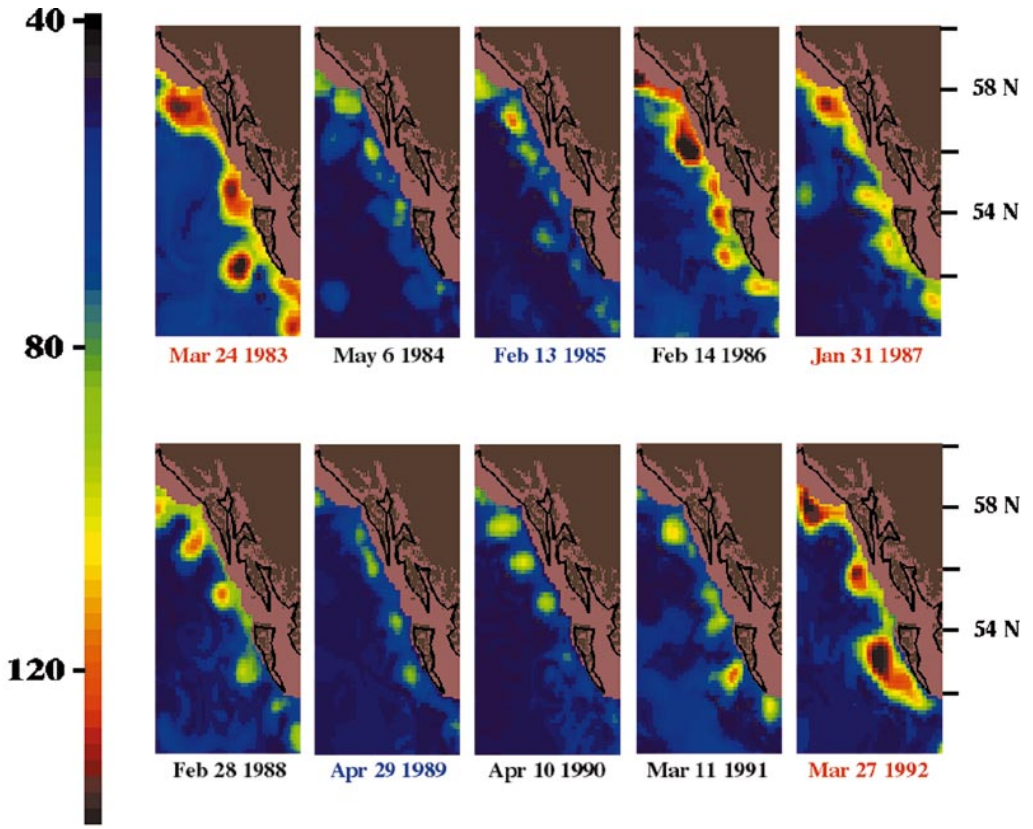

Figure 9. Interannual mesoscale variability. The upper-layer thickness that results from the numerical simulation is displayed when mesoscale features are most evident. Dates in red indicate situations following El Niño events in the tropical Pacific Ocean, whereas dates in blue correspond to El Viejo events. The figure domain extends from 50° to 60°N, and from 140° to 130°W. Snapshot color coding of upper-layer thickness is given by the bar to the left (in m).

are accompanied by a positive SSH anomaly. This fact enables detection of eddies by satellite altimetry provided that the altimeter data have a sufficient accuracy and an adequate horizontal resolution. Thus, observations from the TOPEX/Poseidon and *European Remote Sensing Satellite-2* (*ERS-2*) allow detection of mesoscale motion in the GOA following the most recent major El Niño event that occurred during the 1997–98 boreal winter. As revealed by Figure 10, this El Niño event has also preceded generation of simultaneous multiple anticyclonic eddies in the GOA. These features first appeared in the altimetry records in February 1998, and the eddies have persisted until the time of writing (late November 1998).

The altimeter data have been processed using the geophysical data records of each satellite. The SSH measurements have been corrected for atmospheric effects, removal of tides, inverse barometer pressure loading, and orbit errors. The

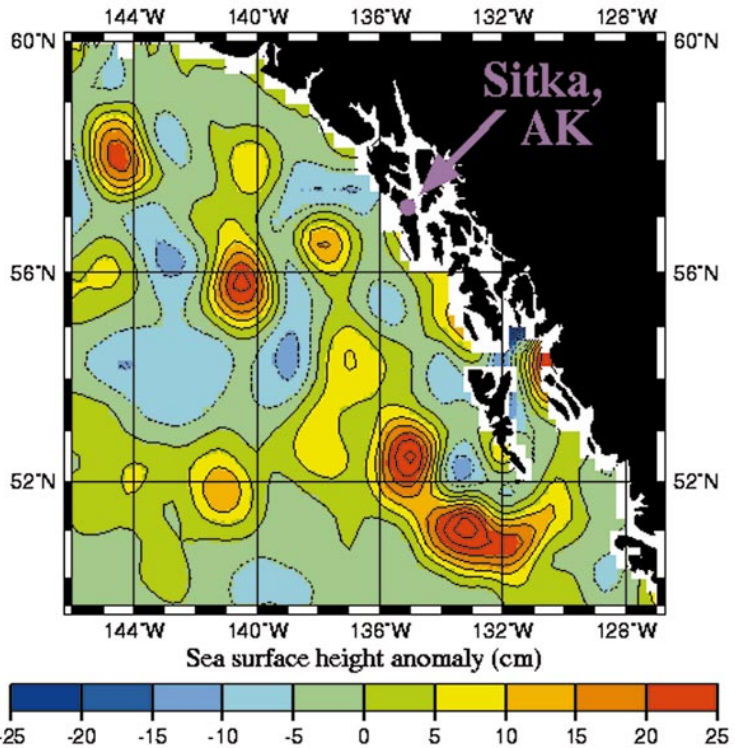

Figure 10. TOPEX/Poseidon and *ERS-2* satellite altimetry analysis for 20 April 1998. Positive and negative anomalies associated with baroclinicity correspond to regions of a deep and shallow upper layer, respectively. The contour line equidistance is 5 cm. (This figure is reproduced with the kind permission of the Colorado Center for Astrodynamics Research, Department of Aerospace Engineering Sciences, University of Colorado, Boulder, CO.)

TOPEX/Poseidon satellite has an alongtrack resolution of approximately 6 km, and a between-track resolution of about 170 km at these latitudes. The corresponding numbers for the *ERS-2* sattelite are 7 km and 23 km, respectively. The repeat cycles are 10 days for TOPEX/Poseidon and 35 days for *ERS-2*.

5. Discussion

Extreme events in the tropical Pacific Ocean affect both the atmospheric and oceanic circulation. It is impossible to formally conclude from these model results alone whether the changes that are seen in the area are due to remote forcing in the ocean through a coastal Kelvin wave teleconnection (Chelton and Davis, 1982) or due to changes in the local atmospheric forcing. Both forcings are present in the model dynamics and it is difficult to separate their independent effects. However, coastal Kelvin waves are clearly observed in the model to propagate

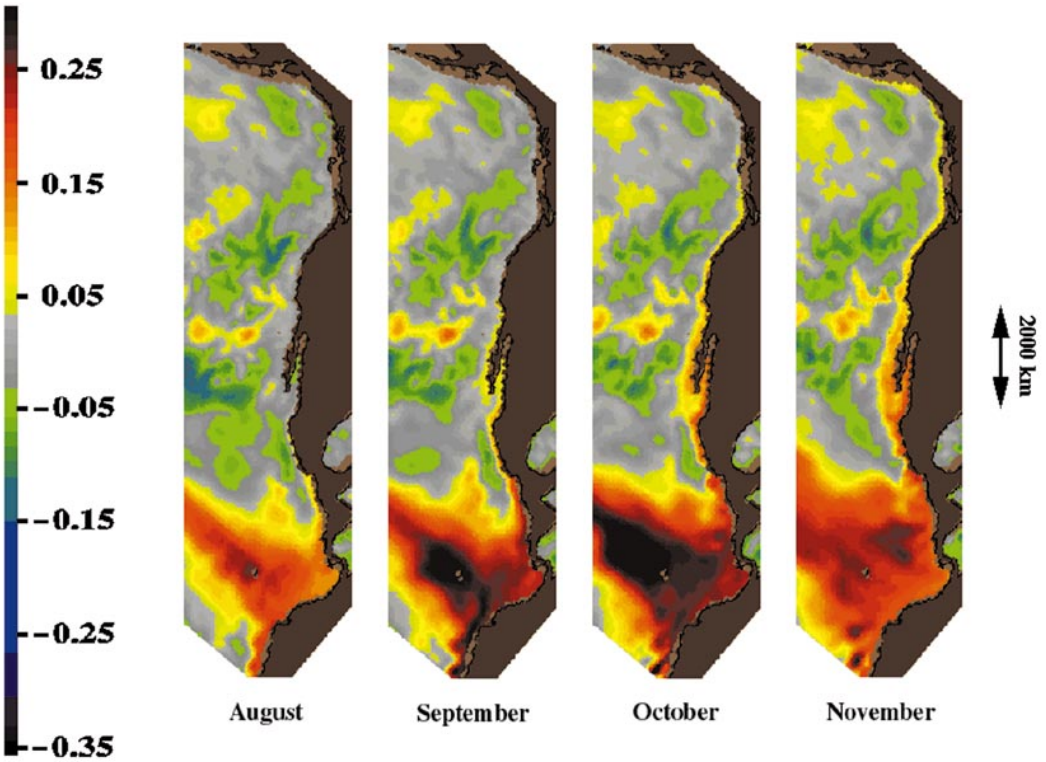

Figure 11. Model generation and propagation of the coastal Kelvin wave during the fall of 1982. SSH along the Pacific coast of Central and North America is displayed for four consecutive months. The color coding of SSH is given by the bar to the left (in m).

from the equatorial Pacific into the GOA. The arrival of a strong downwelling Kelvin wave in the Gulf of Alaska is accompanied by high SSH values (yellow colors in Figure 11), a strengthening of the Alaska Current, and the subsequent formation of warm eddies as the current weakens and starts to move offshore.

The representation of the interannual variability in the model is demonstrated in Figure 12. The LPB filtered anomalies along western North America are shown to be highly correlated at interannual timescales. The onset of El Niño (El Viejo) events, indicated by up arrows (down arrows), precedes rapid increases (decreases) in SSH anomalies at Sitka, Alaska. The dominance of these events in the interannual variability along the coast of the Gulf of Alaska is shown in Figure 13. Keeping in mind that the distance from Neah Bay to Seward is approximately 2000 km, the similarity of the interannual SSH variability along the western coast of North America is remarkable.

Next, we consider the question of whether the SSH variability in this region is generated by winds (local forcing) or by oceanic teleconnections. In Figure 14 the alongshore component of the pseudo–wind stress at 57.5°N, 137.5°W and the observed SSH anomalies at Sitka are depicted after application of a 1-yr LPB

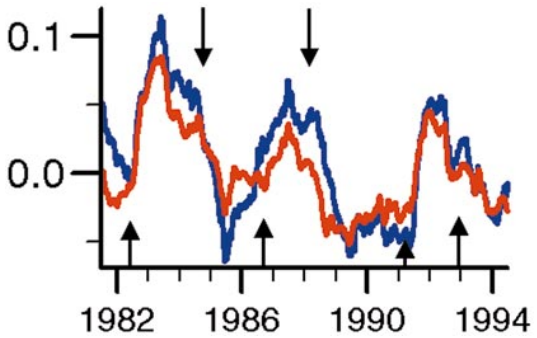

Figure 12. Observed (blue) and modeled (red) SSH anomaly at Sitka, AK, after application of a 1-yr low-pass boxcar filter for the entire duration of the numerical simulation. Numbers on the vertical axes are meters. Anomalies have been computed by subtraction of the 1981–94 mean. Up and down arrows indicate onsets of El Niño and El Viejo events, respectively.

filter. It is obvious from this figure that the anomalously high SSH values reached in early 1983 have not been generated by local winds. Reexamining Figure 13, the 1982–83 SSH anomalies appear to have propagated along the North American coast in a south to north direction, with the largest anomalies in the south. This observation is consistent with a recent study of oceanic teleconnections by coastally trapped Kelvin waves in the equatorial and northeastern Pacific (Meyers et al., 1998). SSH anomalies during 1982–83 are lag correlated up the coast at speeds indicative of Kelvin waves, suggesting the major SSH anomalies of this event are remotely forced in the Tropics and not locally forced by winds. In this way, the major 1982–83 El Niño has affected the ocean circulation along the coasts of the entire American continent. Huyer and Smith (Huyer and Smith, 1985) presented results from observations off Oregon, and concluded that initial anomalies in the sea level and in the hydrography following the 1982–83 El Niño were most plausibly explained by coastal Kelvin waves. Moreover, the high sea level observed at the Oregon coast was subsequently enhanced by local winds. Thus, the Kelvin signal that reached the GOA may have been reinforced by local winds on its path from the equator.

Local wind forcing appears to have affected the interannual variability significantly in the late 1980s and early 1990s. During these years, the SSH anomalies are also somewhat stronger in the northern GOA. This discussion of SSH variability along the GOA coastline supports the results of Emery and Hamilton (Emery and Hamilton, 1985), who found that variations in coastal SSH may be attributed to local winds in some winters, but not all. In particular, they list 1968/69, 1971/72, and 1972/73 as winters with anomalously large SSH without correspondingly strong local winds. It is interesting to note that both 1968/69 and 1972/73 correspond to El Niño events.

The model results for interannual variability of SSH (Figure 12) and me-

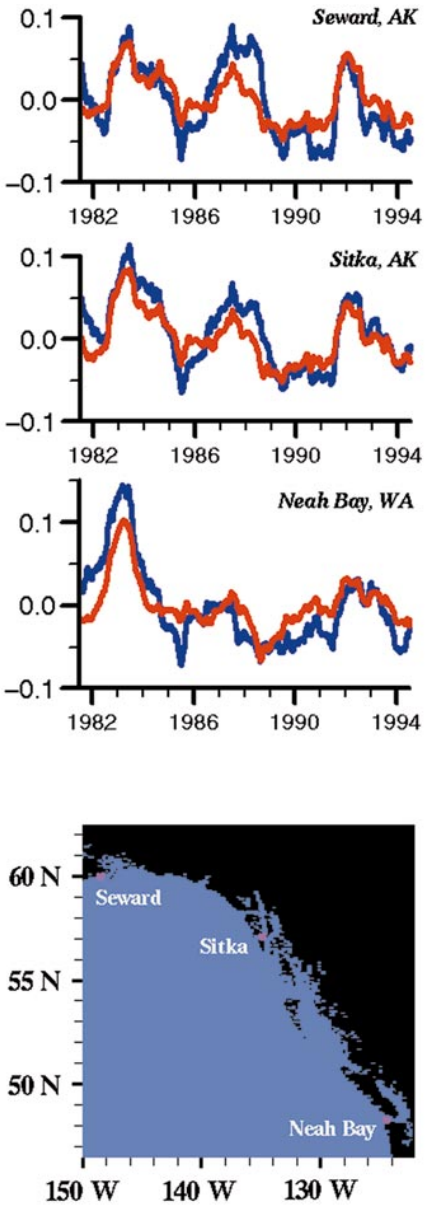

Figure 13. (top) Observed (blue) and modeled (red) SSH anomaly along the northwest coast of North America. Again, seasonal signals have been removed by a 1-yr low-pass boxcar filter. Numbers on the vertical axes are meters. The correlations of 1-yr LPB filtered observed and modeled SSH are 0.82, 0.89, and 0.87 at Seward, Sitka, and Neah Bay, respectively. (bottom) The geographical positions of the three stations under consideration.

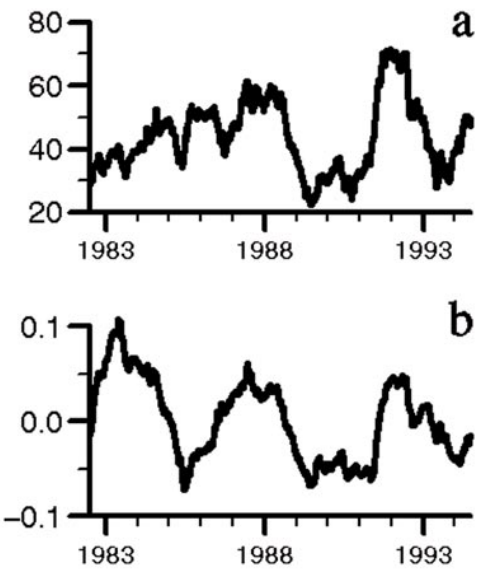

Figure 14. ECMWF pseudo–wind stress alongshore component (top; in $m^2\ s^{-2}$) and observed SSH anomaly (bottom; in m) at Sitka, AK. (The longshore wind component is positive when blowing with land to the right.) A 1-yr low-pass boxcar filter has been applied. SSH anomalies have been computed by subtraction of the 1981–94 mean.

soscale activity (Figure 9) indicate a relationship between these quantities. In a study of anticyclonic eddies in the eastern Mediterranean, it was shown that the growth rate of the most unstable wave is proportional to the maximum speed of the basic-state current (Feliks and Ghil, 1993). This observation may explain the relationship between SSH and mesoscale activity: The model currents are predominantly geostrophic, so large SSH values at the GOA coast correspond to strong currents.

The possible relationship between ENSO events and eddies in the Gulf of Alaska was noted by Swaters and Mysak (Swaters and Mysak, 1985), who suggested that this may be due to variations in the atmospheric circulation of this region linked with such events. The results of the numerical simulation strongly support the hypothesis of a link between ENSO events and intense mesoscale motion in the GOA. The 1982–83 El Niño was one of the major events of the ocean–atmosphere system in the twentieth century and appears to have produced deep eddies in the GOA. The possible link is also seen in the mesoscale activity following the 1991–92 El Niño. On the other hand, the 1986–87 El Niño, which was of moderate size, did not spawn deep eddies in the GOA in the numerical model. Note that the 1986–87 El Niño lasted for more than a year (Meyers and O'Brien, 1995), so the 1988 winter circulation depicted in Figure 9 may also be influenced by ENSO. Note also that the model underrepresents the amplitude of

the 1986–87 El Niño (but not the other two) when forced by the operational ECMWF winds.

From the results for SSH and winds above, we suggest that the deep model eddies generated in early 1983 are predominantly due to oceanic ENSO teleconnections, whereas the deep eddies in 1992 could be influenced by atmospheric teleconnections. The lack of a significant ENSO response in 1986–87 may be due to inadequate ECMWF winds over the equatorial Pacific during this time (Hundermark et al., 1999). Moreover, the local wind forcing contains variability on a decadal timescale that almost certainly has a counterpart in the oceanic variability (Lagerloef, 1995). The present simulation period is unfortunately too short to examine this variability. However, we recall from the discussion in section 4.2 that the correlation between sea level and upper-layer thickness is lower at interannual timescales than at seasonal timescales. This may reflect a decadal variability in the local wind forcing.

Having established NLOM as a numerical model that is suitable for examination of interannual variability in the GOA, our future plans include performing and analyzing a decade-long simulation of the Pacific Ocean with the tropical latitudes excluded. In this way we will be able to discriminate oceanic teleconnections from the equatorial Pacific Ocean during ENSO events. Then, we should be in a better position to be able to distinguish between effects of oceanic and atmospheric teleconnections on the GOA ocean circulation.

The long-term effect of an El Niño event in the North Pacific Ocean circulation was reported based on results from another version of the present numerical model (Jacobs et al., 1994). There it was demonstrated that the 1982–83 El Niño triggered planetary waves that crossed the North Pacific basin and caused a partial northward rerouting of the Kuroshio extension in 1992–93. Computing the empirical orthogonal functions of Geosat altimetry data from the Exact Repeat Mission, Bhaskaran et al. (Bhaskaran et al., 1993) detected a mode in the GOA region for which no cause was found in the local forcing mechanisms. However, the mode, which was strongly reflected in hydrographic data, correlated well with a Southern Oscillation index. This paper demonstrates that the high-latitude ocean responds strongly to ENSO events, having memory over thousands of kilometers and many years. How remotely forced interannual changes in upper-ocean circulation affect marine life or local weather patterns is not fully understood.

Acknowledgments. Financial supported is provided by the Research Council of Norway (Norges Forskningsråd, NFR) and by the Strategic Environmental Research and Development Program (SERDP). The Center for Ocean–Atmosphere Prediction Studies receives its base funding through the Office of Naval Research Secretary of the Navy Chair awarded to Prof. James J. O'Brien. Funding from NFR is provided under Contracts 100674/410 and 122230/720. Funding for the Naval Research Laboratory is provided by the Office of Naval Research under Program Element 62435N, and Advanced Research Projects Agency Grant SC25046 and SERDP. The model simulation was performed on the Cray YMP at the Naval Oceanographic Office, Stennis Space Center, Mississippi. The near–real time and reanalyzed altimeter data were provided by the Colorado Center for Astrodynamics Research at the University of Colorado, Boulder. Thanks to Dr. Detlev Müller for many helpful discussions, and to Prof. Robert R. Leben for generously providing the altimetry image in Figure 10.

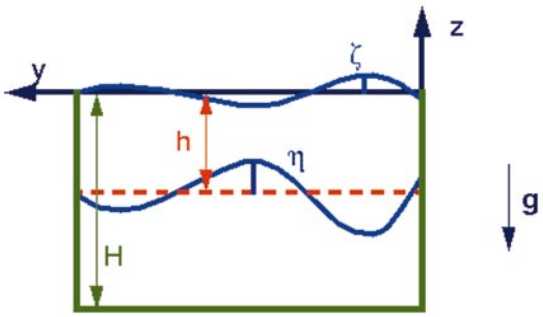

Figure A1. Cross section of the idealized channel that is used for computation of instability growth rates.

Appendix: Stability of Perturbations

A.1 Formulation

We introduce a cross section of the model surface and upper interface into a straight *f*-plane channel as depicted in Figure A1.

First, we define the parameters and variables related to the physical and mathematical description of the present problem. The modification of gravity by stratification is given by

$$\tilde{g} = \frac{\rho_1}{\rho_2} g,$$

$$g^* = \frac{\rho_2 - \rho_1}{\rho_2} g,$$

where the latter definition is customarily referred to as reduced gravity. Then

$$h_1 = h + \zeta - \eta,$$

$$h_2 = H - h + \eta,$$

where h_1 and h_2 are the thicknesses of the top and bottom layers, respectively:

$$u_{1,2}^{\text{total}} = U_{1,2} + u_{1,2}$$

$$v_{1,2}^{\text{total}} = v_{1,2}$$

$$\zeta^{\text{total}} = Z + \zeta$$

$$\eta^{\text{total}} = E + \eta,$$

where u and v are velocities in the x and y directions, respectively. For the right-hand side of these equations, which partition the total quantities, uppercase letters are basic-state quantities, while perturbation quantities are lowercase. Assuming hydrostatic conditions in the vertical and a geostrophically balanced parallel flow,

the basic state is specificed implicitly. The basic-state parallel flow $U(y)$ as a function of surface and interface deflections is given by

$$fU_1 + gZ' = 0$$
$$fU_2 + \tilde{g}Z' + g^*E' = 0$$
$$V_1 = V_2 = 0,$$

where primes denote derivatives of basic-state quantities with respect to y. By perturbing the basic state and keeping only terms that are linear in the perturbed quantities, we can obtain perturbation equations for momentum:

$$u_{1_t} + U_1u_{1_x} + U_1'v_1 - fv_1 + g\zeta_x = 0$$
$$v_{1_t} + U_1v_{1_x} + fu_1 + g\zeta_y = 0$$
$$u_{2_t} + U_2u_{2_x} + U_2'v_2 - fv_2 + \tilde{g}\zeta_x + g^*\eta_x = 0$$
$$v_{2_t} + U_2v_{2_x} + fu_2 + \tilde{g}\zeta_y + g^*\eta_y = 0;$$

for mass

$$(\zeta - \eta)_t + U_1(\zeta - \eta)_x + (h + Z - E)u_{1_x} + (Z - E)'v_1 + (h + Z - E)v_{1_y} = 0$$
$$\eta_t + U_2\eta_x + (H - h + E)u_{2_x} + E'v_2 + (H - h + E)v_{2_y} = 0;$$

and for potential vorticity

$$(v_{1_x} - u_{1_y})_t + U_1(v_{1_x} - u_{1_y}) - U_1''v_1$$
$$- \frac{f - U_1'}{h + Z - E}[(\zeta - \eta)_t + U_1(\zeta - \eta)_x + (Z - E)'v_1] = 0$$
$$(v_{2_x} - u_{2_y})_t + U_2(v_{2_x} - u_{2_y}) - U_2''v_2$$
$$- \frac{f - U_2'}{h + Z - E}[\eta_t + U_2\eta_x + E'v_2] = 0.$$

A version of Phillips's theory for baroclinic instability of a two-layer system is applied (Phillips, 1951). It is assumed that the geostrophic approximation also holds for the perturbation momentum equations, and we are left with the equations for potential vorticity. Perturbations are taken to be represented by Fourier components in x–t space, equivalent to the theory presented in Phillips (Phillips, 1951, pp. 384–385). However, the presence of lateral boundaries requires limitations to be imposed in the y direction:

$$v = A_0e^{i(kx-\sigma t)}\sin l(y-W) \qquad l = \pi/(2D).$$

The form of the other perturbation quantities follows from the perturbation equations for momentum and mass when the simplifications of Phillips's theory are assumed. The quantity W is set to 0 in the right half-channel, and it is set to the channel width in the left half-channel. Note that as in Philips's work (Phillips, 1951), the resulting equations are solved for a given position in the y direction;

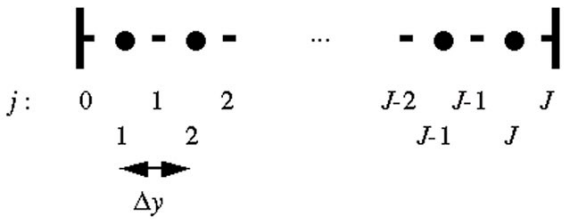

Figure A2. Cross-channel finite difference stencil. Dashes denote *v* nodes, and large dots indicate nodes for *u*/*U* and elevation.

that is, variation in this direction is neglected. The quantity D is then the local distance to the closest channel coast.

A simplifaction in Phillips's publication is that the thicknesses of the two layers are identical. This rather unnecessary approximation is discarded as we assume that the idealized channel has a flat bottom. The channel depth is set to 1000 m, which is an order of magnitude larger than the upper-layer thickness. Finally, we adopt Phillips's simplification of only keeping local values for the basic-state variables in the potential vorticity equations; that is, Taylor series expansion is not applied to the basic state. The growth rate of linear perturbations may then be determined from the dispersion relation, as a function of wavenumber (k) and cross-channel position (y):

$$A\sigma^2 + B\sigma + C = 0$$

$$A = 1 + (v_1 + v_2)/u_0$$

$$B = k[h'_{1;0}(v_2 - v_1) - A(U_{1;0} + U_{2;0})]$$

$$C = k^2[AU_{1;0}U_{2;0} + h'_{1;0}(r_2v_1U_{2;0} - r_1v_2U_{1;0}) - h'^{2}_{1;0}v_1v_2]$$

$$v_i = f/(\kappa^2 h_{i;0}) \qquad \kappa = k^2 + l^2$$

$$u_0 = g^*/f,$$

$$r_i = 1 + v_i/u_0.$$

The second basic-state index (subscript ";0") indicates a constant value.

The approach outlined above has many deficiencies. To eliminate the approximation of using local basic-state values only, we solve the problem using a finite difference formulation for the cross-channel dependence. Given the finite difference stencil shown in Figure A2, we again introduce Fourier perturbations:

$$q = q^*(y)e^{i(kx-\sigma t)},$$

where q is any perturbation quantity and q^* is the cross-channel perturbation shape. The asterisk notation is dropped elsewhere. We can then derive a set of equations for layer 1:

$$kU_1^j u_1^j - \frac{i}{2}[U_1' - f][v_1^j + v_1^{j-1}] + kg\zeta^j = \sigma u_1^j$$

$$\frac{k}{2}[U_1^{j+1} + U_1^j]v_1^j - \frac{if}{2}[u_1^{j+1} + u_1^j] - \frac{ig}{\Delta y}[\zeta_1^{j+1} - \zeta_1^j] = \sigma v_1^j$$

$$kU_1^j\zeta^j + k[U_2^j - U_1^j]\eta^j + k[h - E^j][u_1^j - u_2^j] + k[Z^j u_1^j + Hu_2^j]$$
$$- \frac{i}{2}([Z'^j - E'^j][v_1^j + v_1^{j-1}] + E'^j[v_2^j + v_2^{j-1})]$$
$$- i\frac{h - E^j}{\Delta y}[v_1^j - v_1^{j-1} - v_2^j + v_2^{j-1}]$$
$$- \frac{i}{\Delta y}(Z^j[v_1^j - v_1^{j-1}] + H[v_2^j - v_2^{j-1})] = \sigma\zeta^j,$$

where the superscript denotes stencil index. Observe that the bottom equation is a hybrid of the mass conservation equations where the trend of the interface has been eliminated. Similarly, the set of equations for layer 2 is

$$kU_2^j u_2^j - \frac{i}{2}[U_2' - f][v_2^j + v_2^{j-1}] + k(\tilde{g}\zeta^j + g^*\eta^j) = \sigma u_2^j$$

$$\frac{k}{2}[U_2^{j+1} + U_2^j]v_2^j - \frac{if}{2}[u_2^{j+1} + u_2^j] - \frac{i}{\Delta y}(\tilde{g}[\zeta^{j+1} - \zeta^j] + g^*[\eta^{j+1} - \eta^j]) = \sigma v_2^j$$

$$kU_2^j\eta^j + k[H - h + E^j]u_2^j - \frac{i}{2}E'^j[v_2^j + v_2^{j-1}] - \frac{i}{\Delta y}[H - h + E^j][v_2^j - v_2^{j-1}] = \sigma\eta^j,$$

where, again, the superscript denotes stencil index.

The linear perturbation equations are then transformed to an eigenvalue/eigenvector problem where the imaginary part of eigenvalues correspond to rates of growth/attenuation, and the eigenvectors give the cross-channel perturbation pattern. The finite difference equations may then be solved by conventional utility programs for math problems.

It should be kept in mind that the quality of results hereof are limited by a number of assumptions and simplifications. In the ocean, and in ocean circulation models, features like advection and alongshore dependence of the basic state, coastline and bottom topography, continous/multilayer stratification, and distribution of energy on horizontal scales will all affect the shapes and growth rates of the instabilities.

References

Arakawa, A. 1966. Computational design for long-term numerical integration of the equations of fluid motion: Two-dimensional incompressible flow. Part I. *J. Comput. Phys.*, **12**, 12–35.

Bhaskaran, S., G. S. E. Lagerloef, G. H. Born, W. J. Emery, and R. R. Leben. 1993. Variability in the Gulf of Alaska from Geosat altimetry data. *J. Geophys. Res.*, **98C**, 16,311–16,330.

Chelton, D. B. and R. E. Davis. 1982. Monthly mean sea level variability along the west coast of North America. *J. Phys. Oceanogr.*, **12**, 757–784.

Cummins, P. F. and L. A. Mysak. 1988. A quasi-geostrophic model of the northeast Pacific. Part I: A preliminary numerical experiment. *J. Phys. Oceanogr.*, **18**, 1261–1286.

Eady, E. A. 1949. Long waves and cyclone waves. *Tellus*, **1**, 33–52.

Emery, W. J. and K. Hamilton. 1985. Atmospheric forcing of interannual variability in the northeast Pacific Ocean: Connections with El Niño. *J. Geophys. Res.*, **90C**, 857–868.

Enfield, D. and J. S. Allen. 1980. On the structure and dynamics of monthly mean sea level anomalies along the Pacific coast of North and South America. *J. Phys. Oceanogr.*, **10**, 557–578.

Feliks, Y. and M. Ghil. 1993. Downwelling-front instability and eddy formation in the eastern Mediterranean. *J. Phys. Oceanogr.*, **23**, 61–78.

Fjørtoft, R. 1950. Application of integral theorems in deriving criteria of stability for laminar flows and for the baroclinic circular vortex. *Geofys. Publ.*, Vol. 17, No. 6, 52–78.

Hellerman, S. and M. Rosenstein. 1983. Normal monthly wind stress over the world ocean with error estimates. *J. Phys. Oceanogr.*, **13**, 1093–1104.

Hoskins, B. J. 1975. The geostrophic momentum approximation and the semi-geostrophic equations. *J. Atmos. Sci.*, **32**, 233–242.

Hundermark, B. W., H. E. Hurlburt, E. J. Metzger, and J. F. Shriver. 1999. A comparison of wind stresses derived from ECMWF 1000 mb winds and FSU pseudo stresses over the tropical Pacific Ocean, 1981–1993. *Tech. Rep. NRL/FR/7323-95-9643,* Naval Research Laboratory, Stennis Space Center, MS, in press..

Hurlburt, H. E. and J. D. Thompson. 1980. A numerical study of loop current intrusions and eddy shedding. *J. Phys. Oceanogr.*, **10**, 1611–1651.

Hurlburt, H. E., A. J. Wallcraft, W. J. Schmitz Jr., P. J. Hogan, and E. J. Metzger. 1996. Dynamics of the Kuroshio/Oyashio Current system using eddy-resolving models of the North Pacific Ocean. *J. Geophys. Res.*, **101C**, 941–976.

Huyer, A. and R. L. Smith. 1985. The signature of El Niño off Oregon, 1982–1983. *J. Geophys. Res.*, **90C**, 7133–7142.

Jacobs, G. A., H. E. Hurlburt, J. C. Kindle, E. J. Metzger, J. L. Mitchell, W. J. Teague, and A. J. Wallcraft. 1994. Decade-scale trans-Pacific propagation and warming effects of an El Niño anomaly. *Nature*, **370**, 360–363.

Johnson, M. A. and J. J. O'Brien. 1990. The northeast Pacific Ocean response to the 1982–1983 El Niño. *J. Geophys. Res.*, **95C**, 7155–7166.

Kuo, H. L. 1949. Dynamic instability of two-dimensional nondivergent flow in a barotropic atmosphere. *J. Meteorol.*, **6**, 165–185.

Lagerloef, G. S. E. 1995. Interdecadal variations in the Alaska Gyre. *J. Phys. Oceanogr.*, **25**, 2242–2258.

Lagerloef, G. S. E., R. D. Muench, and J. D. Schumacher. 1981. Low-frequency variations in currents near the shelf break: Northeast Gulf of Alaska. *J. Phys. Oceanogr.*, **11**, 627–638.

Martinsen, E. A., B. Gjevik, and L. P. Røed. 1979. A numerical model for long barotropic waves and storm surges along the western coast of Norway. *J. Phys. Oceanogr.*, **9**, 1126–1138.

McGowan, J. A. 1985. El Niño 1983 on the Southern California bight. *El Niño North: El Niño Effects in the Eastern Subarctic Pacific Ocean,* W. S. Wooster and D. L. Fluharty University of Washington Sea Grant Publ., 166–184.

Metzger, E. J., H. E. Hurlburt, J. C. Kindle, R. C. Rhodes, G. A. Jacobs, J. F. Shriver, and O. M. Smedstad. 1998. The 1997 El Niño in the NRL Layered Ocean Model. *NRL Review*, Naval Research Laboratory, Washington, DC. 63–71.

Meyers, S. D. and J. J. O'Brien. 1995. Pacific Ocean influences atmospheric carbon dioxide. *Eos Trans. AGU*, **76**, 1.

Meyers, S. D., M. A. Johnson, M. Liu, J. J. O'Brien, and J. L. Spiesberger. 1996. Interdecadal variability in a numerical model of the northeast Pacific Ocean. 1970–89. *J. Phys. Oceanogr.*, **26**, 2635–2652.

Meyers, S. D., A. Melsom, G. T. Mitchum, and J. J. O'Brien. 1998. Detection of the fast Kelvin wave teleconnections due to ENSO. *J. Geophys. Res.*, **103C**, 27,655–27,663.

Meyers, S. D., J. J. O'Brien, and E. Thelin. 1999. Reconstruction of monthly SST in the tropical Pacific Ocean during 1868-1993 using adaptive climate basis functions. *Mon. Weather Rev.*, in press..

Moore, D. W. 1968. Planetary–gravity waves in an equatorial ocean. Ph.D. thesis, Harvard University, Cambridge, MA. 207 pp..

Mysak, L. A. 1985. On the interannual variability of eddies in the northeast Pacific Ocean. *El Niño North: El Niño Effects in the Eastern Subarctic Pacific Ocean,* W. S. Wooster and D. L. Fluharty University of Washington Sea Grant Publ., 97–106.

NOAA. cited 1988. Digital relief of the surface of the earth. *Data Announcement 88-MGG-02,* National Geophysics Data Center, Boulder, CO. [Available at: http://www.ngdc.noaa.gov:80/mgg/global/etopo5.HTML].

Norton, J. G. and D. R. McLain. 1994. Diagnostic patterns of seasonal and interannual temperature variation off the west coast of the United States: Local and remote large-scale atmospheric forcing. *J. Geophys. Res.*, **99C**, 16,019–16,030.

Pares-Sierra, A. and J. J. O'Brien. 1989. The seasonal and interannual variability of the California Current system: A numerical model. *J. Geophys. Res.*, **94C**, 3159–3180.

Phillips, N. A. 1951. A simple three-dimensional model for the study of large-scale extratropical flow patterns. *J. Meteorol.*, **8**, 381–394.

Ramp, S. R., J. L. McClean, C. A. Collins, A. J. Semtner, and K. A. S. Hays. 1997. Observations and modeling of the 1991–1992 El Niño signal off central California. *J. Geophys. Res.*, **102C**, 5553–5582.

Rayleigh, Lord 1880. On the stability, or instability, of certain fluid motions. *Proc. London Math. Soc.*, **9**, 57–70.

Royer, T. C. 1975. Seasonal variations of water in the northern Gulf of Alaska. *Deep Sea Res.*, **22**, 403–416.

Shriver, J. F. and H. E. Hurlburt. 1997. The contribution of the global thermohaline circulation to the Pacific to Indian Ocean throughflow via Indonesia. *J. Geophys. Res.*, **102C**, 5491–5511.

Smedstad, O. M., D. N. Fox, H. E. Hurlburt, G. A. Jacobs, E. J. Metzger, and J. L. Mitchell. 1997. Altimeter data assimilation into a 1/8° eddy resolving model of the Pacific Ocean. *J. Meteorol. Soc. Jpn.*, **75**, 429–444.

Smith, P. E. 1985. A case history of an anti-El Niño to El Niño transition on plankton and nekton distribution and abundances. *El Niño North: El Niño effects in the Eastern Subarctic Pacific Ocean,* W. S. Wooster and D. L. Fluharty University of Washington Sea Grant Publ., 121–142.

Spillane, M. C., D. B. Enfield, and J. S. Allen. 1987. Intraseasonal oscillations in sea level along the west coast of the Americas. *J. Phys. Oceanogr.*, **17**, 313–325.

Swaters, G. E. and L. A. Mysak. 1985. Topographically induced baroclinic eddies near a coast, with application to the northeast Pacific. *J. Phys. Oceanogr.*, **15**, 1470–1485.

Tabata, S. 1982. The anticyclonic, baroclinic eddy off Sitka, Alaska, in the northeast Pacific Ocean. *J. Phys. Oceanogr.*, **12**, 1260–1282.

Thomson, R. E., and J. F. R. Gower. 1998. A basin-scale oceanic instability event in the Gulf of Alaska. *J. Geophys. Res.*, **103C**, 3033–3040.

Walker, G. T. 1928. World weather. *Q. J. R. Meteorol. Soc.*, **54**, 79–87.

Wallace, J. M. and D. S. Gutzler. 1981. Teleconnections in the geopotential height field during Northern Hemisphere winter. *Mon. Weather Rev.*, **109**, 784–812.

Wallcraft, A. J. 1991. The Navy layered ocean model users' guide. *NOARL Rep. 35,* Naval Research Laboratory, Stennis Space Center, MS 21 pp.

Ware, D. M. and R. E. Thomson. 1991. Link between long-term variability in upwelling and fish production in the northeast Pacific Ocean. *Fish. Ocean.*, **48**, 2296–2306.

Table 1. Correlations of observed and modeled SSH at Sitka. The 1-yr periods considered are centered at new year. Lags are in days with positive lags corresponding to observations leading model results. Years followed by "**w**" and "**c**" correspond to El Niño events and El Viejo events, respectively. Here we have used the ENSO definision by Meyers and O'Brien (1995), which is based on Galapagos sea level anomalies.

Period	3.05 sample Lag	2-month LPB filter Correlation	Lag	Correlation
1981–82	3	0.67	24	0.93
1982–83**w**	3	0.78	15	0.99
1983–84	3	0.58	12	0.83
1984–85**c**	3	0.67	43	0.90
1985–86	3	0.73	−6	0.94
1986–87**w**	9	0.75	12	0.97
1987–88	3	0.75	12	0.93
1988–89**c**	3	0.42	6	0.33
1989–90[1]	46	0.61	46	0.94
1990–91	6	0.58	9	0.61
1991–92**w**	3	0.79	18	0.97
1992–93	3	0.64	6	0.86
1993–94[2]**w**	9	0.66	15	0.96

[1] There is also a local correlation maximum of 0.48 at a lag of 3 days in the 1989–90 3.05 sample case.
[2] This El Niño event commences in December 1992, but it probably had its strongest influence in the GOA in 1993–94 due to the delayed signal at distant latitudes.